Magneto-optical trapping using planar optics

William R. McGehee,[1,2,†] Wenqi Zhu,[1,2] Daniel S. Barker,[1,3] Daron Westly,[1] Alexander Yulaev,[1,4] Nikolai Klimov,[1] Amit Agrawal,[1,2] Stephen Eckel,[1] Vladimir Aksyuk,[1] and Jabez J. McClelland[1]

[1]Physical Measurement Laboratory, National Institute of Standards and Technology, Gaithersburg, MD 20899, USA
[2]Institute for Research in Electronics and Applied Physics and Maryland NanoCenter, University of Maryland, College Park, MD 20742, USA
[3]Joint Quantum Institute, University of Maryland, College Park, MD 20742, USA
[4]Department of Chemistry and Biochemistry, University of Maryland, College Park, MD 20742, USA
[†]Present address: Physical Measurement Laboratory, National Institute of Standards and Technology, Boulder, CO 80305, USA

E-mail: william.mcgehee@nist.gov

Abstract

Laser-cooled atoms are a key technology for many calibration-free measurement platforms—including clocks, gyroscopes, and gravimeters—and are a promising system for quantum networking and quantum computing. The optics and vacuum hardware required to prepare these gases are often bulky and not amenable to large-volume manufacturing, limiting the practical realization of devices benefiting from the properties of cold atoms. Planar, lithographically produced optics including photonic integrated circuits, optical metasurfaces, and gratings offer a pathway to develop chip-scale, manufacturable devices utilizing cold atoms. As a demonstration of this technology, we have realized laser cooling of atomic Rb in a grating-type magneto-optical trap (MOT) using planar optics for beam launching, beam shaping, and polarization control. Efficient use of available light is accomplished using metasurface-enabled beam shaping, and the performance of the planar optics MOT is competitive with Gaussian-beam illuminated grating MOTs.

Keywords: laser cooling, metasurfaces, photonic integrated circuits

1. Introduction

Measurements utilizing gases of laser-cooled atoms are presently confined to controlled laboratory environments due to the large optical assemblies required to prepare and manipulate cold gases. Methods for miniaturization, simplification, and integration of laser-cooling technology will impact applications including clocks[1–4], inertial sensors[5–7], magnetometers[8], vacuum sensors[9], quantum simulation[10], and quantum networking[11]. Preparing atoms into a magneto-optical trap (MOT) is a key step in these applications, and efforts to miniaturize MOT designs have centered around replacing conventional 6-beam designs[12] with single-input-beam alternatives such as pyramid MOTs[13–15] and grating MOTs (GMOTs)[16,17]. While these methods provide significant simplification of the optical hardware required for laser cooling, it is desirable to achieve a laser-cooling platform composed of planar nanophotonic components which can be lithographically fabricated and integrated to form a portable, manufacturable package[18–20].

Advances in near-infrared and visible spectrum planar optics have enabled significant progress toward realizing a planar optics MOT[21]. Lithographically fabricated grating chips have broadened the scope of GMOT design[16,22] including the realization of integrated Zeeman-slowing[23], grating-based two-dimensional (2D) MOTs[24], and new methods for trapping alkaline earth atoms[25]. Photonic integrated circuits (PIC) fabricated on SiN_x platforms have enabled chip-based interrogation of warm atomic vapors for clock applications[3,26] as well as accurately focused beams to interface with trapped ions for quantum information processing[27]. Recent works have demonstrated a beam-launching architecture for laser cooling using PIC-based large-area grating mode converters[28] and laser-cooling using a metasurface (MS) optic for beam splitting[29].

In this work, we demonstrate laser cooling using a collection of planar optical elements operating at 780 nm to form a GMOT of ^{87}Rb. We begin by coupling free-space light into a nanophotonic waveguide on a PIC (Fig. 1). The challenge in realizing this MOT is in efficiently converting the sub-micrometer waveguide mode in the PIC into a free-space mode of centimeter-scale, a change in mode area by a factor $\approx 10^{10}$. Beam expansion is necessary as magneto-optical trapping is inefficient with millimeter-scale or smaller laser beams due to the finite optical scattering forces present in laser cooling[12]. It is also necessary to increase the capture rate into the MOT, which scales strongly with the size of the laser cooling beams[22]. We employ a multi-stage approach to expand the

waveguide mode using the combination of an extreme mode-converter (EMC) on the PIC and a transmissive, dielectric metasurface acting as an aspheric beam-shaper. The shaped free-space beam impinges on a segmented, reflective grating chip (Fig. 1(b)) which diffracts light into three additional beams to form a four-beam GMOT within a conventional glass vacuum chamber.
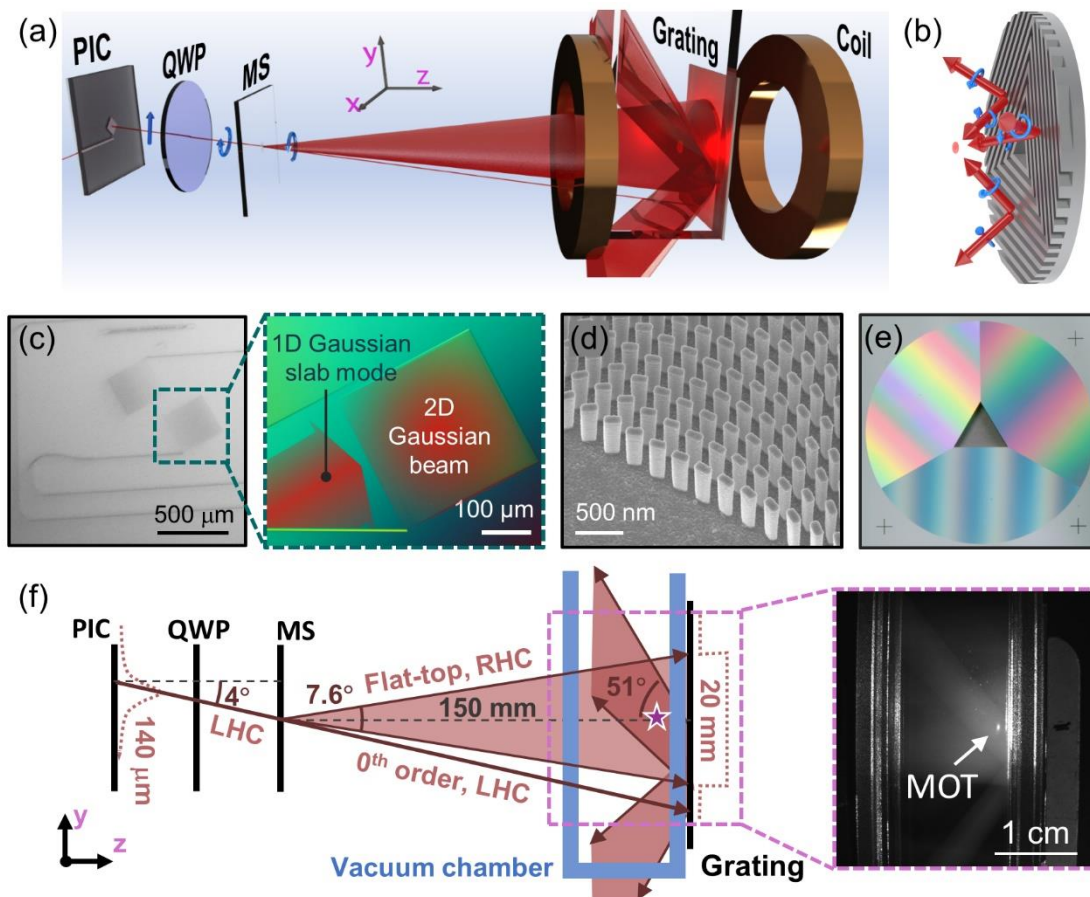

Fig. 1. Planar optics GMOT apparatus. (a) A linearly polarized Gaussian beam (red line) is launched from the PIC and circularly polarized using a QWP. The MS generates an expanding mode of opposite polarization (red cone) which realizes a flat-top intensity profile at the segmented grating chip. Three first-order diffracted beams, one from each grating segment, overlap with the incident light to form the four-beam GMOT. Positive and negative first order diffraction from one grating segment is shown. The GMOT is realized inside a glass vacuum chamber with a magnetic quadrupole field created by external electromagnets. (b) Illustration of first order diffraction and beam polarization (blue arrows) from the grating chip. (c) Optical image of PIC shows waveguide and EMC structures. Inset illustrates components of the EMC. (d) Scanning electron micrograph shows MS pillars which generate the polarization-dependent phase profile. (e) Optical image of three-segment grating chip; ruled region has 22 mm diameter. (f) Cross-section of (**a**) provides detailed geometry of the apparatus. Dotted red lines indicate Gaussian and flat-top intensity profiles. Beam polarizations are left-hand (LHC) and right-hand circular

(RHC). Star point indicates GMOT position. Inset shows atomic fluorescence at 780 nm from the GMOT and the laser-cooling beams at Rb partial pressure of $\approx 1 \times 10^{-4}$ Pa.

2. Design and characterization of planar optics

To form a MOT using planar optics, we manipulate the laser cooling light with a PIC, MS, and a grating chip as shown in Fig. 1. The PIC projects a linearly polarized Gaussian beam at $\approx 4°$ from normal to the PIC surface (Fig. 1(f)), and a quarter-wave plate (QWP) converts the beam polarization to circular. The beam strikes the transmissive, dielectric MS at $4°$ from normal. The MS phase profile causes the beam to deflect normal to the MS and to diverge such that a flat-top intensity profile is realized after expanding over ≈ 150 mm distance. At this distance, the beam is ≈ 20 mm in diameter and impinges on a three-segment diffraction grating chip. The grating chip (Fig. 1(b)) diffracts light at $\approx 51°$ (the 1st diffraction order at normal incidence) at 780 nm. Three diffracted beams, one from each grating segment, overlap with the flat-top mode within a glass-walled vacuum chamber to form the laser-cooling volume of the GMOT. External electromagnets generate a quadrupole magnetic field whose center resides in the laser beam overlap volume. The arrangement of the overlapping beams and the quadrupole magnetic field provides confining forces both along the z-axis and in the radial (x-y) plane of the GMOT. The glass cell is attached to a chamber containing an ion pump and a Rb dispenser used to generate adjustable partial pressures of Rb.

The SiN_x-based PIC (Fig. 1(c)), which launches the Gaussian beam into free space, is composed of a waveguide and an EMC similar to the design described in Refs. [30,31]. The PIC is fabricated from a 250 nm thick layer of nominally stoichiometric silicon nitride (SiN_x) clad from both sides in 3 μm of silicon dioxide (SiO_2) with photonic structures defined using electron-beam lithography followed by reactive-ion etching. Light is edge-coupled into the fundamental TE_0 mode of a waveguide of 250 nm × 300 nm cross-section, aided by an inverse taper at the edge of the chip that adiabatically expands the optical mode to increase coupling efficiency of free-space light into the waveguide. Light is guided ≈ 5 mm across the chip to the EMC where it is evanescently coupled into a SiN_x slab mode and then scattered into free-space using an apodized grating structure where it forms a circular, collimated Gaussian beam with an $1/e^2$ radius of ≈ 140 μm at an angle of $\approx 4°$ from the surface normal (along the negative-y axis). In the EMC, both the slab-mode coupling and the apodized grating scattering rate are spatially varied to

project the desired collimated, 2D Gaussian intensity profile, increasing the mode area by a factor of $\approx 10^5$. The total power efficiency of the PIC from input to output beam is ≈ 9 % with input and output coupling losses of ≈ 6.5 dB and ≈ 3 dB, respectively. The free-space linearly polarized beam from the PIC is converted to circular polarization using a conventional QWP (Fig. 1).

The Pancharatnam-Berry (PB) type MS[32], composed of dielectric Si pillars (Fig 1(d)), converts the PIC-launched Gaussian beam into a diverging beam with half angle of 3.8°, such that a flat-top intensity profile is realized at a distance $d \approx 150$ mm, and redirects the beam normal to the MS optic with a deflection angle of 4°, as shown in Fig. 1(f). The divergence enables the beam to fill a circular region of radius $R \approx 10$ mm, matching the ruled region of the grating chip (Fig. 2), after expanding over the 150 mm distance. The flat-top intensity realized at the grating surface provides uniform illumination of the grating chip, such that the generated optical forces from the incident and diffracted beam are approximately balanced across the laser-cooling volume. The 4° deflection allows spatial separation from the 0th order transmission and ensures a uniform polarization state of the expanding beam.
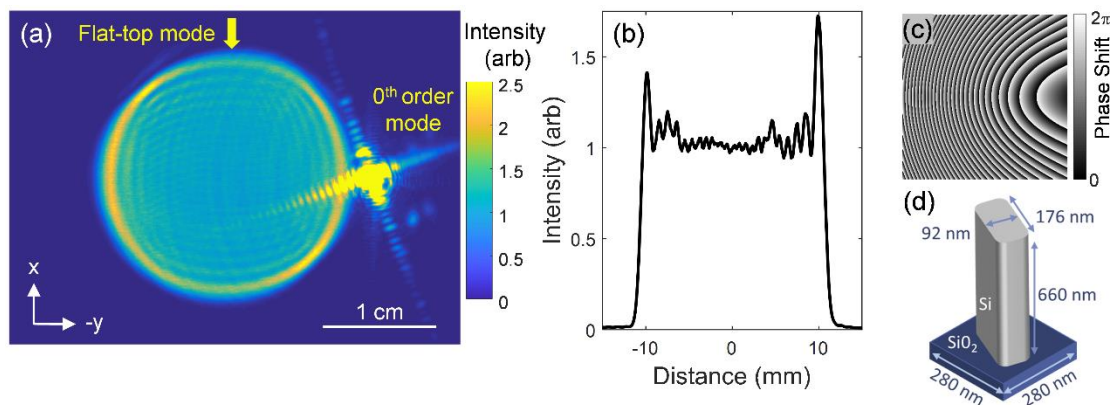

Fig. 2. Characterization of the flat-top laser beam. (a) Intensity of the flat-top and 0th order modes ≈ 150 mm from the MS, equivalent to the location of the grating chip. (b) Slice of the intensity profile along the *x*-axis [yellow arrow in (a)] shows uniformity of the flat-top mode. (c) Computed phase profile of the MS optic including the beam-shaping and prism phase contributions. MS area is 300 μm × 300 μm. (d) Schematic of MS unit cell with quarter-wave phase pillar. In-plane rotation of the pillar sets the local geometrical phase shift of the light.

The MS, similar to the work described in Ref. [33], is constructed from rectangular, polycrystalline Si nanopillars supported by a fused-silica substrate. The pillars reside on a square grid with 280 nm spacing covering an area of

300 μm × 300 μm. The pillars (Fig. 2(d)) have nominal in-plane dimensions of 92 nm × 176 nm and a constant height of 660 nm. The geometry of Si pillars which compose the MS have shape-birefringence such that each pillar acts as a half-wave retarding element for 780 nm light (the wavelength of the Rb cooling transitions). Circularly polarized light incident on these structures has its polarization handedness reversed and receives a local geometrical phase shift set by the pillars' in-plane rotational orientation. The pillar-orientation-dependent phase shift is used to generate the desired phase profile. The metasurface is mounted above the QWP and spatially centered on the PIC-launched beam.

The phase profile encoded on the MS is the planar equivalent to a prism followed by a non-spherical, negative focal length lens. The phase profile is determined using a ray optics approach assuming that the local phase gradients ϕ' in the planar optic will deflect normally incident light at an angle θ_z from normal as $\sin(\theta_z) = \frac{\lambda}{2\pi n}\phi'$, where λ is the vacuum wavelength of light and n is the effective index of the propagating medium. The radially symmetric phase gradient, which maps the power in an ideal Gaussian beam of $1/e^2$ radius w uniformly into a circle of radius R at a distance d from the MS, can be expressed as:

$$\frac{d\phi}{dr} = \frac{2\pi n}{\lambda}\frac{1}{\sqrt{1+\frac{d^2}{\left(R\sqrt{1-e^{-\frac{2r^2}{w^2}}}-r\right)^2}}}. \quad (1)$$

This phase profile is not stationary in propagation, and the flat-top intensity is realized in a region around the design distance d away from the MS which includes the GMOT capture volume. The 4° deflection is achieved using an additional linear phase ramp along the *y*-axis of the metasurface and spatially separates the flat-top mode from the undesired 0th order transmission at the grating location. The composite phase profile exiting the metasurface is plotted in Fig. 2(c).

The intensity profile of the flat-top beam is measured at the location of the diffraction grating (Fig. 2(a)). The flat-top mode achieves the desired 10 mm radius at 150 mm expansion distance and achieves high uniformity over the mode area (Fig. 2(c)). Root-mean-squared (RMS) intensity variations are observed at $\approx$ 7 % in the central 20 % of the mode area and < 20 % over the central 80 % of the mode area. Two lobes with peak intensities $\approx$ 2.5× the central mode intensity are formed on the periphery of the flat-top mode due to the $\approx$ 4° incidence angle of the PIC-

launched beam with the MS. These lobes likely alter the total GMOT capture rate. The balance of forces at the location of the trapped atoms is minimally impacted by these lobes as they do not significantly overlap within this volume. Ripples in the mode profile arise both from diffractive effects during beam propagation as well as spatially varying diffraction efficiency and optical absorption across the MS, primarily at the location of phase discontinuities. Separation between the flat-top mode and the 0th order beam is necessary as the peak intensity of the unshaped, 0th order beam is $\approx 100\times$ higher than that of the flat-top mode at this location. The intense, 0th order beam would distort or destroy the GMOT if they were to significantly overlap. High-order diffraction is seen in the 0th order beam due to clipping of the Gaussian profile in the EMC.

The MS has an experimentally measured conversion efficiency into the flat-top mode of ≈ 71 %. The efficiency is limited by several factors including Fresnel reflection, optical absorption in Si due to above-bandgap operation, fabrication imperfections, and lithographic limits on the number of sub-wavelength elements that can be placed within an optical wavelength. Other MS types, including designs based on propagation phase[33], could be used to generate the desired circular polarization and phase profile simultaneously without requiring the QWP. Variations in absorption and diffraction, including the effect of phase discontinuities, exist in all MS types and lead to spatial structure in the output beam intensity. For the divergent beam we are creating, undesired spatial structure in the beam's intensity formed at the MS will persist as the beam propagates due to the beam's significant divergence. Such non-ideal intensity variations are detrimental to the GMOT performance, however the PB-type MS utilized here offers acceptable variation in absorption and diffraction across the surface of the device[34]. We note that while we have chosen to use separate elements for the EMC and MS, direct integration of metasurfaces with the EMC is possible and has been demonstrated in Ref. [33].

The grating-chip is composed of three, 120º oriented one-dimensional diffraction gratings (Fig. 1(e)). First order diffraction from the gratings opposes the incident beam to provide both axial and radial confining forces, realizing a four-beam geometry GMOT[35]. The grating chip is fabricated from Al-coated Si as described in Ref. [23] with periodic square grooves arranged with a nominal pitch of 1 µm and trench width of 500 nm. The ruled grating pattern fills a circular region with diameter of 22 mm. A triangular opening with an inscribed circular diameter of 3 mm is etched through the center of the grating chip to eliminate reflected light along the beam axis. First order

diffraction for normally incident light at 780 nm occurs at $\approx 51.3°$ with a diffraction efficiency of ≈ 33 %. The diffraction angle is chosen to provide a balance between axial and radial confining forces, providing a nearly spherical GMOT as shown in Fig. 3. The optimal diffraction efficiency of 1/3 is approximated by controlling the etch depth and duty cycle of the grating as described in Ref. [16]. The grating is mounted *ex vacuo* parallel to the wall of the vacuum cell and normal to the diverging flat-top laser beam. The GMOT forms ≈ 5 mm away (negative *z*-direction) from the inside surface of the glass chamber wall (Fig. 1(f)). The overlap of the incident and diffracted beams forms a GMOT trapping volume $V_{trap} \approx 0.34$ cm^3, partially restricted by the 4 mm wall thickness of the vacuum chamber.
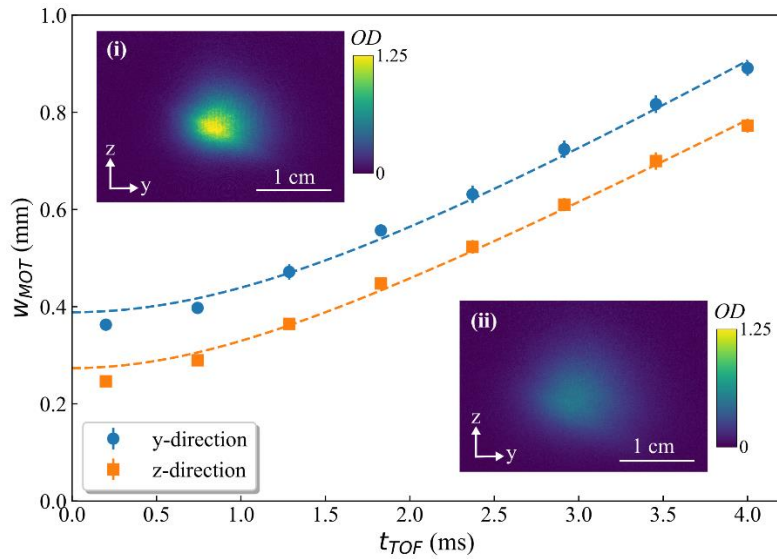

Fig. 3. Time-of-flight temperature measurement. Temperature of the GMOT is ≈ 200 μK at $I_{trap}/I_{sat} \approx 0.5$. Insets show absorption images at t_{TOF} = (i) 1.8 ms and (ii) 3.5 ms.

The GMOT is formed using the D_2 transitions in ^{87}Rb. Laser cooling light is prepared using standard methods to address the $5S_{1/2} \longrightarrow 5P_{3/2}$, F = 2 $\longrightarrow$ F' = 3 (trapping) and F = 1 $\longrightarrow$ F' = 2 (repumping) transitions near 780.24 nm [12]. The laser-cooling beams are combined and coupled into the PIC waveguide using fiber and free-space optics to match the ≈ 0.93 μm $1/e^2$ mode radius at the waveguide facet. The transitions (separated by ≈ 6.6 GHz) have natural linewidths Γ of $\approx 2\pi \times 6.1$ MHz and the trapping light has a saturation intensity $I_{sat} \approx 3.6$ mW cm^{-2}. Imaging of the GMOT is performed along an optical path orthogonal to the flat-top beam axis (*x*-direction in Fig. 1). The loading rate of the GMOT is measured using fluorescence imaging while atom number and temperature are

measured using absorption imaging in time-of-flight (TOF). Absorption imaging measures the optical depth (OD) of the gas, proportional to the atomic column density, as the natural logarithm of the ratio of incident to transmitted optical intensity. During TOF expansion and imaging, the GMOT electromagnets and MOT optical fields are switched off. A permanent magnet creates an $\approx 50~\mu T$ field along the x-direction to serve as a spin quantization axis for imaging.

3. Characterization of planar optics GMOT

We have realized a GMOT using the D_2 transitions in [87]Rb and the planar optics described above. Capture into the GMOT is maximized when the trapping light detuning is $\approx -1.5~\Gamma$ and the axial gradient of the magnetic quadrupole field is $\approx 0.11~T~m^{-1}$, consistent with values reported in Ref. [22]. Repumping light, copropagating with the trapping light, is resonant to the repumping transition and has a central intensity of $25~\mu W~cm^{-2}$ for all measurements. In the low intensity limit, the trapped gas has an approximately Gaussian shape with $1/e^2$ radii (w_{MOT}) of $270~\mu m$ axially and $390~\mu m$ radially. The dimensions of the gas increase with I_{trap} as the total GMOT population grows, and the radial-to-axial aspect ratio saturates to 2 at high trapping light intensity.

At the maximum trapping light intensity $I_{trap} \approx 1.8~mW~cm^{-2}$ ($\approx 0.5~I_{sat}$), the GMOT loading rate measured using fluorescence imaging is $\approx 10^7~s^{-1}$ with a trapping lifetime of $\approx 0.25~s$, consistent with a background Rb partial pressure of $8 \times 10^{-7}~Pa$[36]. The gas temperature measured using time-of-flight absorption imaging is $(176 \pm 5)~\mu K$ in the axial direction and $(219 \pm 7)~\mu K$ in the radial direction (Fig. 3). Here, uncertainties are the standard uncertainty of the mean. The measured temperature is close to the [87]Rb D_2 Doppler cooling limit of $146~\mu K$[37], and the axis-dependent temperature is a consequence of the force balance set by the diffraction angle of the grating chip[38]. Lower temperatures would be achievable using additional cooling stages including polarization-gradient cooling[39] or Λ-enhanced grey molasses[40].

The steady-state population of the GMOT (N_{MOT}) is characterized at varying trapping laser intensities. We observe that N_{MOT} grows in an approximately linear fashion starting from near 0 population at $I_{trap} \approx 0.45~mW~cm^{-2}$ and reaches a population of $\approx 2.8 \times 10^6$ at $I_{trap} \approx 1.8~mW~cm^{-2}$ (Fig. 4). The GMOT population below $I_{trap} = 0.5~mW~cm^{-2}$ is minimal due to a combination of decreased scattering forces and increased trap loss at low I_{trap}[41,42]. Linear

growth of atom number with I_{trap} is typical at low saturation of the atomic transition, and maximum steady-state GMOT populations are typically observed at $I_{trap} >> I_{sat.}$ For comparison, N_{MOT} in Ref. [22] was observed to peak at 6×10^7 using $I_{trap} \approx 50$ mW cm^{-2} (≈ 14 I_{sat}) in $V_{trap} \approx 1$ cm^3. The same work demonstrated a volume scaling $N_{MOT} \sim V_{trap}^{1.2}$, predicting an equivalent maximum N_{MOT} of 1.8×10^7 atoms in our system ($V_{trap} = 0.34$ cm^3, star point in Fig. 4 inset). The volume-scaled population is consistent with our observed GMOT population trend.
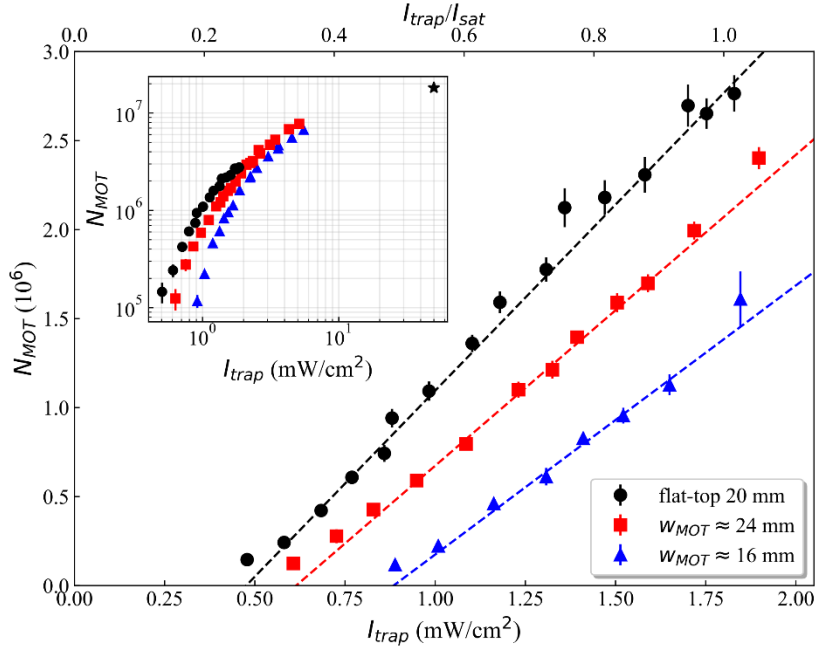

Fig. 4. Steady-state GMOT population *vs.* cooling light intensity. Data are shown for 20 mm diameter, flat-top illumination of the grating chip (black circles) as well as apodized Gaussian beam illumination with $w \approx 24$ mm (red squares) and $w \approx 16$ mm (blue triangles). Dashed lines are linear fits to the data below 2 mW cm^{-2}. Inset shows the same data over a larger intensity range. Extrapolated population using GMOT performance and volume scaling in Ref. [22] is plotted for $V_{trap} \approx 0.34$ cm^3 (black star).

4. Comparison to Gaussian-illuminated GMOT

We compare the performance of the planar-optics, flat-top illuminated GMOT to traditional, Gaussian-beam illuminated GMOTs. A bulk-optics assembly is used to prepare collimated, circularly polarized Gaussian beams normally incident to the grating chip. Two beam waists (intensity $1/e^2$ radii) of $w \approx 16$ mm and ≈ 24 mm are tested. Each Gaussian beam impinges at normal incidence on the segmented grating chip and is apodized within a 20 mm diameter circle to match the boundary size of the 20 mm diameter flat-top beam. The concomitant beam overlap

volume approximates that of the flat-top beam GMOT and enables a fair comparison of their relative performance. GMOTs are prepared using the same nominal laser frequencies, quadrupole field gradient, and Rb partial pressure used in the flat-top illuminated GMOT. The intensity of the trapping light is varied (quoted using the Gaussian beam's central intensity), and atom number and temperature measurements are made using TOF imaging. Measured temperatures and in-trap sizes are consistent with the flat-top illuminated GMOT values.

The Gaussian-illuminated GMOT population is lower than that observed with flat-top illumination as shown in Fig. 4. For Gaussian illumination, the onset of appreciable capture is also observed at non-zero laser intensity and N_{MOT} also increases approximately linearly in the low-saturation regime. Reduced capture rate for Gaussian illumination is expected due to decreased optical forces at the periphery of the capture volume and to imperfect balancing of laser-cooling forces arising from the Gaussian intensity profile[38]. Accordingly, the onset intensity of the linear population trends also shifts to higher intensity for smaller w. Zero N_{MOT} intercept values of $I_{trap} \approx 0.48$ mW cm^{-2}, $I_{trap} \approx 0.61$ mW cm^{-2}, and $I_{trap} \approx 0.88$ mW cm^{-2} are observed for the flat-top, $w \approx 24$ mm and $w \approx 16$ mm beams, respectively. The shift to capture beginning at higher central beam intensity corresponds roughly to equal intensities averaged over the trapping volume. Mean intensities over the trapping volume are calculated to be ≈ 110 %, ≈ 84.7 %, and ≈ 77 % of I_{trap} for the flat-top, w = 24 mm, and w = 16 mm beams, respectively. The population reduction with Gaussian illumination is most pronounced in the low saturation regime in which optical forces are linearly related to intensity. At high values of I_{trap}, the observed N_{MOT} trends for flat-top and Gaussian illumination begin to converge due to saturation of the atomic transition as shown in Fig. 4 inset.

5. Discussion

Use of the MS-generated flat-top beam allows for efficient use of the available optical power in illuminating the grating chip. Uniform illumination in a GMOT ensures that diffracted light from the grating segments can balance the forces created from the incident beam. In Gaussian-beam illuminated GMOTs, this is typically accomplished using beam waists of similar or larger dimension than the clear aperture of the grating[9,43]. Light falling outside of the grating aperture is wasted—for the $w \approx 24$ mm beam used here, ≈ 30 % of the light strikes the ruled grating area and ≈ 2.5 times the optical power is required to observe the onset of trapping (accounting for the ≈ 71 %

efficiency of the MS). Similarly, ≈ 2.5 times more optical power is required for the $w \approx 24$ mm beam to trap 10^6 atoms relative to the flat-top beam. Further improvements in power efficiency could be obtained through more complex MS-enabled beam shaping.

The absolute power efficiency of the planar optics in generating the divergent flat-top beam from a fiber-launched Gaussian beam is ≈ 6.4 % (≈ 12 dB loss). Coupling light into and projecting light from the PIC is the largest source of loss at ≈ 10.5 dB due to a combination of insertion loss into the PIC, waveguide loss, and scattering into the PIC substrate in the EMC. Similar devices have demonstrated losses as low as 7.5 dB $\pm$ 0.5 dB using fiber edge coupling [30], and significant improvement in the mode coupler efficiencies are possible with more complex designs. The MS efficiency corresponds to ≈ 1.5 dB loss and is competitive with other high-performance designs[44]. The grating design is also a source of lost optical power as, by design, only 1/3 of the incident light is diffracted toward the capture volume. Schemes using large area metasurfaces or PIC-based beam launching for all required beams provide paths to potentially higher power efficiency at the expense of greater experimental complexity.

Physical size is also a limitation of the planar optics GMOT presented here for the realization of small, cold atom-based devices. Within the GMOT geometry, reduction of the beam expansion distances (increasing the beam divergence) introduces several effects that complicate the balancing of optical forces in the GMOT including round-trip expansion of the beam, spatial variation in diffraction efficiency across the grating chip, and non-uniform geometrical compression of the diffracted beams. Incident-angle dependence of the diffracted polarization state can also arise, though this is measured to be minimal for our grating chip. For the 3.8° half-divergence angle (150 mm expansion distance) used here, the divergent mode sufficiently approximates a collimated beam at the grating to allow for use of uniform-pitch grating chip and formation of the GMOT. Steeper divergence angles could be accommodated using gratings with spatially-varying pitch and curvature designed to compensate for the angle-dependent effects, enabling the possibility of millimeter-scale separation between the MS and the grating chip in such designs. The finite forces available in laser cooling limit miniaturization beyond the millimeter scale.

6. Conclusion

We have demonstrated a GMOT of Rb using planar optical elements including a PIC, MS, and grating chip to launch and manipulate light for laser cooling. Bridging the gap between the sub-micrometer-scale guided mode on the PIC and the centimeter-scale beam needed for laser cooling, a magnification of the mode area by $\approx 10^{10}$, is accomplished using an on-chip EMC to launch a Gaussian mode into free space as well as a beam-shaping, polarization-dependent MS to generate an expanding, flat-top mode laser beam. The flat-top beam efficiently illuminates a grating chip to realize a four-beam GMOT with capture rates demonstrated as high as $\approx 10^7$ s^{-1} and gas temperatures below 200 μK. Steady-state GMOT populations were demonstrated at $\approx 2.8 \times 10^6$, consistent with published volume and intensity scaling for GMOT performance[22]. Comparisons to equivalent Gaussian-beam-illuminated GMOTs demonstrate the power efficiency of the flat-top beam profile relative to conventional Gaussian-illumination.

The GMOT geometry and planar optics demonstrated here offer a natural pathway toward realizing calibration-free measurement platforms and other quantum devices utilizing laser-cooled atoms. The demonstrated architecture is compatible with further integration with on-chip light sources, solid-state alkali dispensers[45], MEMS-based vacuum hardware[46,47], and on-chip methods for imaging, and improvements in near-infrared and visible spectrum photonic integrated circuits will make these devices more power efficienct and expand the scope of addressable atoms. We hope that the small physical size and robustness of planar optics GMOT designs will enable compact atomic clock designs, the emerging role of cold atoms in space interferometry for test of fundamental physics[48,49], and components required for widespread quantum networking.

Acknowledgements

References

[1]   Hummon M T, Kang S, Bopp D G, Li Q, Westly D A, Kim S, Fredrick C, Diddams S A, Srinivasan K, Aksyuk V and Kitching J E 2018 Photonic chip for laser stabilization to an atomic vapor with 10^{-11} instability *Optica* **5** 443–9

[2]   Martin K W, Phelps G, Lemke N D, Bigelow M S, Stuhl B, Wojcik M, Holt M, Coddington I, Bishop M W and Burke J H 2018 Compact Optical Atomic Clock Based on a Two-Photon Transition in Rubidium *Phys. Rev. Applied* **9** 014019

[3]   Newman Z L, Maurice V, Drake T, Stone J R, Briles T C, Spencer D T, Fredrick C, Li Q, Westly D, Ilic B R, Shen B, Suh M-G, Yang K Y, Johnson C, Johnson D M S, Hollberg L, Vahala K J, Srinivasan K, Diddams S A, Kitching J, Papp S B and Hummon M T 2019 Architecture for the photonic integration of an optical atomic clock *Optica* **6** 680–5

[4]   Elvin R, Hoth G W, Wright M, Lewis B, McGilligan J P, McGilligan J P, Arnold A S, Griffin P F and Riis E 2019 Cold-atom clock based on a diffractive optic *Opt. Express* **27** 38359–66

[5]   Becker D, Lachmann M D, Seidel S T, Ahlers H, Dinkelaker A N, Grosse J, Hellmig O, Müntinga H, Schkolnik V, Wendrich T, Wenzlawski A, Weps B, Corgier R, Franz T, Gaaloul N, Herr W, Lüdtke D, Popp M, Amri S, Duncker H, Erbe M, Kohfeldt A, Kubelka-Lange A, Braxmaier C, Charron E, Ertmer W, Krutzik M, Lämmerzahl C, Peters A, Schleich W P, Sengstock K, Walser R, Wicht A, Windpassinger P and Rasel E M 2018 Space-borne Bose–Einstein condensation for precision interferometry *Nature* **562** 391

[6]   Bongs K, Holynski M, Vovrosh J, Bouyer P, Condon G, Rasel E, Schubert C, Schleich W P and Roura A 2019 Taking atom interferometric quantum sensors from the laboratory to real-world applications *Nature Reviews Physics* **1** 731–9

[7]   Geiger R, Landragin A, Merlet S and Pereira Dos Santos F 2020 High-accuracy inertial measurements with cold-atom sensors *AVS Quantum Sci.* **2** 024702

[8]   Behbood N, Martin Ciurana F, Colangelo G, Napolitano M, Mitchell M W and Sewell R J 2013 Real-time vector field tracking with a cold-atom magnetometer *Appl. Phys. Lett.* **102** 173504

[9]   Eckel S, Barker D S, Fedchak J A, Klimov N N, Norrgard E, Scherschligt J, Makrides C and Tiesinga E 2018 Challenges to miniaturizing cold atom technology for deployable vacuum metrology *Metrologia* **55** S182–S193

[10]   Straatsma C J E, Ivory M K, Duggan J, Ramirez-Serrano J, Anderson D Z and Salim E A 2015 On-chip optical lattice for cold atom experiments *Opt. Lett.* **40** 3368–71

[11]   Yu Y, Ma F, Luo X-Y, Jing B, Sun P-F, Fang R-Z, Yang C-W, Liu H, Zheng M-Y, Xie X-P, Zhang W-J, You L-X, Wang Z, Chen T-Y, Zhang Q, Bao X-H and Pan J-W 2020 Entanglement of two quantum memories via fibres over dozens of kilometres *Nature* **578** 240–5

[12]   Phillips W D 1998 Nobel Lecture: Laser cooling and trapping of neutral atoms *Rev. Mod. Phys.* **70** 721–41

[13]   Arlt J J, Maragò O, Webster S, Hopkins S and Foot C J 1998 A pyramidal magneto-optical trap as a source of slow atoms *Optics Communications* **157** 303–9

[14]   Noh H-R and Jhe W 2002 Atom optics with hollow optical systems *Physics Reports* **372** 269–317

[15]   Bowden W, Hobson R, Hill I R, Vianello A, Schioppo M, Silva A, Margolis H S, Baird P E G and Gill P 2019 A pyramid MOT with integrated optical cavities as a cold atom platform for an optical lattice clock *Scientific Reports* **9**

[16]   McGilligan J P, Griffin P F, Riis E and Arnold A S 2016 Diffraction-grating characterization for cold-atom experiments *J. Opt. Soc. Am. B* **33** 1271–7

[17]   Kitching J 2018 Chip-scale atomic devices *Applied Physics Reviews* **5** 031302

[18]   Rushton J A, Aldous M and Himsworth M D 2014 Contributed Review: The feasibility of a fully miniaturized magneto-optical trap for portable ultracold quantum technology *Review of Scientific Instruments* **85** 121501

[19]   Keil M, Amit O, Zhou S, Groswasser D, Japha Y and Folman R 2016 Fifteen years of cold matter on the atom chip: promise, realizations, and prospects *Journal of Modern Optics* **63** 1840–85

[20]   Birkl G, Buchkremer F B J, Dumke R and Ertmer W 2001 Atom optics with microfabricated optical elements *Optics Communications* **191** 67–81

[21]   Blumenthal D J 2020 Photonic integration for UV to IR applications *APL Photonics* **5** 020903

[22]   Nshii C C, Vangeleyn M, Cotter J P, Griffin P F, Hinds E A, Ironside C N, See P, Sinclair A G, Riis E and Arnold A S 2013 A surface-patterned chip as a strong source of ultracold atoms for quantum technologies *Nature Nanotechnology* **8** 321–4

[23]   Barker D S, Norrgard E B, Klimov N N, Fedchak J A, Scherschligt J and Eckel S 2019 Single-Beam Zeeman Slower and Magneto-Optical Trap Using a Nanofabricated Grating *Phys. Rev. Applied* **11** 064023

[24]   Imhof E, Stuhl B K, Kasch B, Kroese B, Olson S E and Squires M B 2017 Two-dimensional grating magneto-optical trap *Phys. Rev. A* **96** 033636

[25]   Sitaram A, Elgee P K, Campbell G K, Klimov N N, Eckel S and Barker D S 2020 Confinement of an alkaline-earth element in a grating magneto-optical trap *Review of Scientific Instruments* **91** 103202

[26]   Stern L, Bopp D G, Schima S A, Maurice V N and Kitching J E 2019 Chip-scale atomic diffractive optical elements *Nature Communications* **10** 1–7

[27]   Mehta K K, Zhang C, Malinowski M, Nguyen T-L, Stadler M and Home J P 2020 Integrated optical multi-ion quantum logic *Nature* **586** 533–7

[28]   Chauhan N, Bose D, Puckett M, Moreira R, Nelson K and Blumenthal D J 2019 Photonic Integrated Si3N4 Ultra-Large-Area Grating Waveguide MOT Interface for 3D Atomic Clock Laser Cooling *Conference on Lasers and Electro-Optics (2019), paper STu4O.3* CLEO: Science and Innovations (Optical Society of America) p STu4O.3

[29]   Zhu L, Liu X, Sain B, Wang M, Schlickriede C, Tang Y, Deng J, Li K, Yang J, Holynski M, Zhang S, Zentgraf T, Bongs K, Lien Y-H and Li G 2020 A dielectric metasurface optical chip for the generation of cold atoms *Science Advances* **6** eabb6667

[30]   Kim S, Westly D A, Roxworthy B J, Li Q, Yulaev A, Srinivasan K and Aksyuk V A 2018 Photonic waveguide to free-space Gaussian beam extreme mode converter *Light: Science & Applications* **7** 72

[31]   Yulaev A, Kim S, Westly D A, Roxworthy B J, Li Q, Srinivasan K A and Aksyuk V A 2018 Collimating a Free-Space Gaussian Beam by Means of a Chip-Scale Photonic Extreme Mode Converter *2018 International Conference on Optical MEMS and Nanophotonics (OMN)* 2018 International Conference on Optical MEMS and Nanophotonics pp 1–2

[32]   Bomzon Z, Kleiner V and Hasman E 2001 Pancharatnam–Berry phase in space-variant polarization-state manipulations with subwavelength gratings *Opt. Lett.* **26** 1424–6

[33]   Yulaev A, Zhu W, Zhang C, Westly D A, Lezec H J, Agrawal A and Aksyuk V 2019 Metasurface-Integrated Photonic Platform for Versatile Free-Space Beam Projection with Polarization Control *ACS Photonics* **6** 2902–9

[34]   Sell D, Yang J, Doshay S, Yang R and Fan J A 2017 Large-Angle, Multifunctional Metagratings Based on Freeform Multimode Geometries *Nano Lett.* **17** 3752–7

[35]   Vangeleyn M, Griffin P F, Riis E and Arnold A S 2009 Single-laser, one beam, tetrahedral magneto-optical trap *Opt. Express* **17** 13601–8

[36]   Arpornthip T, Sackett C A and Hughes K J 2012 Vacuum-pressure measurement using a magneto-optical trap *Phys. Rev. A* **85** 033420

[37]   Lett P D, Phillips W D, Rolston S L, Tanner C E, Watts R N and Westbrook C I 1989 Optical molasses *J. Opt. Soc. Am. B, JOSAB* **6** 2084–107

[38]   McGilligan J P, Griffin P F, Riis E and Arnold A S 2015 Phase-space properties of magneto-optical traps utilising micro-fabricated gratings. *Opt. Express* **23** 8948–59

[39]   Lee J, Grover J A, Orozco L A and Rolston S L 2013 Sub-Doppler cooling of neutral atoms in a grating magneto-optical trap *J. Opt. Soc. Am. B* **30** 2869–74

[40]   Rosi S, Burchianti A, Conclave S, Naik D S, Roati G, Fort C and Minardi F 2018 Λ-enhanced grey molasses on the D2 transition of Rubidium-87 atoms *Sci Rep* **8**

[41]   Wallace C D, Dinneen T P, Tan K-Y N, Grove T T and Gould P L 1992 Isotopic difference in trap loss collisions of laser cooled rubidium atoms *Phys. Rev. Lett.* **69** 897–900

[42]   Weiner J, Bagnato V S, Zilio S and Julienne P S 1999 Experiments and theory in cold and ultracold collisions *Rev. Mod. Phys.* **71** 1–85

[43]   McGilligan J P, Griffin P F, Elvin R, Ingleby S J, Riis E and Arnold A S 2017 Grating chips for quantum technologies *Scientific Reports* **7**

[44]   Devlin R C, Khorasaninejad M, Chen W T, Oh J and Capasso F 2016 Broadband high-efficiency dielectric metasurfaces for the visible spectrum *PNAS* **113** 10473–8

[45]   McGilligan J P, Moore K R, Kang S, Mott R, Mis A, Roper C, Donley E A and Kitching J 2020 Dynamic Characterization of an Alkali-Ion Battery as a Source for Laser-Cooled Atoms *Phys. Rev. Applied* **13** 044038

[46]   McGilligan J P, Moore K R, Dellis A, Martinez G D, de Clercq E, Griffin P F, Arnold A S, Riis E, Boudot R and Kitching J 2020 Laser cooling in a chip-scale platform *Appl. Phys. Lett.* **117** 054001

[47]   Squires M B, Olson S E, Kasch B, Stickney J A, Erickson C J, Crow J A R, Carlson E J and Burke J H 2016 Ex vacuo atom chip Bose-Einstein condensate *Appl. Phys. Lett.* **109** 264101

[48]   Trimeche A, Battelier B, Becker D, Bertoldi A, Bouyer P, Braxmaier C, Charron E, Corgier R, Cornelius M, Douch K, Gaaloul N, Herrmann S, Müller J, Rasel E, Schubert C, Wu H and Santos F P dos 2019 Concept study and preliminary design of a cold atom interferometer for space gravity gradiometry *Class. Quantum Grav.* **36** 215004

[49]   Loriani S, Schlippert D, Schubert C, Abend S, Ahlers H, Ertmer W, Rudolph J, Hogan J M, Kasevich M A, Rasel E M and Gaaloul N 2019 Atomic source selection in space-borne gravitational wave detection *New J. Phys.* **21** 063030